International Journal of Heat and Fluid Flow 112 (2025) 109672

Contents lists available at ScienceDirect

International Journal of Heat and Fluid Flow

journal homepage: www.elsevier.com/locate/ijhff

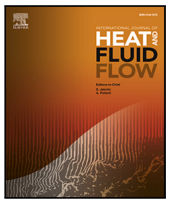

Aspect-ratio effect on the wake of a wall-mounted square cylinder immersed in a turbulent boundary layer

Gerardo Zampino [a,*], Marco Atzori [b], Elias Zea [c], Evelyn Otero [d], Ricardo Vinuesa [a]

[a] FLOW Engineering Mechanics, KTH Royal Institute of Technology, Stockholm, Sweden
[b] Dipartimento di Scienze e Tecnologie Aerospaziali, Politecnico di Milano, Milan, Italy
[c] MWL Engineering Mechanics, KTH Royal Institute of Technology, Stockholm, Sweden
[d] CSA Engineering Mechanics, KTH Royal Institute of Technology, Stockholm, Sweden

ARTICLE INFO

Dataset link: https://www.vinuesalab.com/databases/

Keywords:
Wall-mounted square cylinder
Turbulent boundary layer
Critical aspect ratio

ABSTRACT

The wake topology behind a wall-mounted square cylinder immersed in a turbulent boundary layer is investigated using high-resolution large-eddy simulations (LES). The boundary-layer thickness at the obstacle location is fixed, with a Reynolds number based on cylinder height h and free-stream velocity u_∞ of 10,000 while the aspect ratio (AR), defined as obstacle height divided by its width, ranges from 1 to 4. The mesh resolution is comparable to DNS standards used for similar wall-mounted obstacles, though with relatively lower Reynolds numbers. The effects of AR on wake structures, turbulence production, and transport are analyzed via Reynolds stresses, anisotropy-invariant maps (AIM), and the turbulent kinetic energy (TKE) budget. In particular, the transition from "dipole" to a "quadrupole" wake is extensively examined as AR increases. With increasing AR, the wake shrinks in both the streamwise and spanwise directions, attributed to the occurrence of the base vortices (AR = 3 and 4). This change in the flow structure also affects the size of the positive-production region that extends from the roof and the flank of the obstacle to the wake core. The AIMs confirm three-dimensional wake features, showing TKE redistribution in all directions (Simonsen and Krogstad, 2005). Stronger turbulence production in AR = 3 and 4 cases highlights the role of tip and base vortices behind the cylinder. The overall aim is to refine the dipole-to-quadrupole transition as a function of AR and accounting for the incoming TBL properties. The novelty relies on proposing the momentum-thickness-based Reynolds number Re_θ as a discriminant for assessing TBL effects on turbulent wake structures.

1. Introduction

The study of turbulent structures around wall-mounted cylinders has gained increased attention from the scientific community due to the higher similarities with the urban environment. Predicting turbulent flows around buildings becomes relevant for environmental purposes and new technology implementations. In the past decades, both numerical and experimental studies in the literature have discussed the behavior of near-wake structures as a function of the aspect ratio (AR), as the ratio between cylinder height and diameter (Sakamoto and Arie, 1983; Zhang et al., 2017), the Reynolds number (Zhao et al., 2021), the turbulence of the incoming flow (Vinuesa et al., 2015), the boundary-layer thickness (Chen et al., 2022; El Hassan et al., 2015) and the cross-section shape (Kumar and Tiwari, 2019; Rastan et al., 2021), that makes a comprehensive parametric study of the wake regimes difficult.

In recent studies, Wang and Zhou (2009) offered a detailed explanation of the time-averaged wake turbulent structures behind a wall-mounted cylinder as a synthesis of three primary structures: tip, base, and spanwise vortices. The tip vortices are a couple of counter-rotating vortices developing at the free end of the cylinder roof and producing a strong downwash in the wake. In proximity to the base, a second pair of counter-rotating vortices develop with an opposite sense of rotation in respect to the tip vortices. The base vortices are inclined upwards and they produce a strong upwash in the lower portion of the wake. Both tip and base vortices extend in the streamwise direction downstream the cylinder and were used by Wang and Zhou (2009) to distinguish between a "dipole", showing only the footprint of the tip vortices, and "quadrupole" configuration, where both tip and base vortices are observed. However, as further discussed by Zhang et al. (2017), the base vortices weaken downstream and the "quadrupole" in the near-wake region changes into a "dipole" configuration. In addition, Wang and Zhou (2009) defined the spanwise vortices as the two vertical turbulent filaments separating at the side of the obstacle, connected by a horizontal bridge to form an arch-type vortex. Upstream the cylinder a horseshoe vortex has been identified as an elongated

* Corresponding author.
E-mail address: gzampino@kth.se (G. Zampino).

https://doi.org/10.1016/j.ijheatfluidflow.2024.109672
Received 9 April 2024; Received in revised form 21 November 2024; Accepted 21 November 2024
Available online 10 December 2024

Nomenclature

Abbreviations

AIM	Anisotropy-invariant map
AR	Aspect Ratio
CR	Cross-sectional aspect ratio
IR	Isolated roughness
SF	Skimming flow
TKE	Turbulent kinetic energy
WI	Wake interference

English symbols

$\overline{u_i' u_j'}$	i-jth Reynolds stress term.
Re_τ	Friction Reynolds number
Re_θ	Momentum-thickness-based Reynolds number
Re_h	Bulk-velocity-based Reynolds number
Re_{δ^*}	Displacement-thickness-based Reynolds number
d	Cylinder width
h	Cylinder height
k	Turbulent kinetic energy
L_x, L_y, L_z	Length of the numerical domain in the x, y and z directions.
u_τ	Friction velocity

Greek symbols

Δ	Mean element size $= (\Delta x \Delta y \Delta z)^{1/3}$
δ^*	Displacement thickness
δ_{99}	Boundary-layer thickness
ϵ	Isotropic dissipation
η	Kolmogorov scale defined as $\eta = (\nu^3/\epsilon)^{1/4}$
ν	Kinematic viscosity
θ	Momentum thickness

Other symbols

$.^+$	Inner scaled quantity
$\bar{.}$	Time-averaged quantity
$\tilde{.}$	Filtered quantity

vortical structure that occurs at the junction between the cylinder and the bottom surface due to the adverse pressure gradient induced by the obstacle blockage (Sumner et al., 2004).

However, not all authors concur with this interpretation. For example, Sakamoto and Arie (1983) hypothesized that the flow separating from the roof of the cylinder creates a turbulent filament that bridges the spanwise vortices from the flank of the cylinder producing an arch-type vortex. The tip and base vortices are thus its footprint in a vertical section. More recently Bourgeois et al. (2011) proposed a fully connected wake interpratation. Two vertical principal cores occur at the lateral edge of the buildings and both sides are connected by a horizontal "connector strand" (Bourgeois et al., 2011, 2012). The distinction between "dipole" and "quadrupole" wake configurations depends on the presence of two looped or half-looped vortices oscillating behind the obstacle. Finally, in order of publication, Zhang et al. (2017) observed a third wake configuration known as "Six-Vortices Type", where six poles develop behind the obstacle. Another model is the hairpin vortex model by Dousset and Pothérat (2010), which describes the instantaneous wake. According to this model, the wake behind the obstacle can be distinguished as symmetric vortex shedding for lower AR values, and as an antisymmetric wake for large AR values. The "legs" at the sides of the cylinders form a "C" shape in any horizontal plane within the wake. Moving downstream, the two ends of the "C" shape are deflected upstream forming the "Reverse-C" spanwise vortices (Zhang et al., 2017). These latter turbulent structures transit to the hairpin vortices due to the fragmentation of large pieces of vortices because of the interaction between the boundary layer, the shear layer, and the downwash produced by the free end of the cylinder (Zhang et al., 2017).

Despite differing interpretations and models recently proposed in the literature, it is consolidated that turbulent structures downstream of a wall-mounted cylinder vary with the AR (Wang and Zhou, 2009; Bourgeois et al., 2012; Porteous et al., 2014; Yauwenas et al., 2019). For AR below a critical value AR_c, the time-averaged wake exhibits a dipole configuration with a couple of counter-rotating tip vortices. The instantaneous wake exhibits a symmetric Kármán vortex shedding (Zhang et al., 2017). For increasing AR, above the critical value, the base vortices emerges and the instantaneous field becomes antisymmetric. The vortex topology plays a crucial role in influencing the production and distribution of wake turbulence (Atzori et al., 2023) and a comprehensive understanding of this phenomenon is furthermore necessary. Although the estimated AR_c relies between 2 and 6 (Sakamoto and Arie, 1983; Kawamura et al., 1984; Sumner et al., 2004; Wang and Zhou, 2009), universally agreed-upon definition is still missing in literature since it depends on many factors, such as the turbulence characteristics of the incoming flow (Vinuesa et al., 2015), the boundary-layer thickness (Hosseini et al., 2013; El Hassan et al., 2015; Chen et al., 2022) and the cross-sectional aspect ratio (CR) (Rastan et al., 2021). Regarding the turbulence properties, Goswami and Hemmati (2022) reported a similar transition from the dipole to a quadrupole wake for relatively low Reynolds number and for a laminar boundary layer. Although the generation mechanism of the tip and base vortices is the same for both laminar and turbulent boundary layer, Goswami and Hemmati (2022) motivated the early transition for a turbulent boundary layer due to the flow instabilities inherent to a turbulent flow. The cross-sectional aspect ratio (CR), defined as the ratio between the cylinder's longitudinal length and width, was observed by Rastan et al. (2021) to have a more significant effect on wake structures than AR. For CR = 1, the wake is characterized by two streamwise vortices originating from side edges, forming a dipole configuration. With increasing CR, the flow reattaches to the top surface, creating a separation bubble that merges with streamwise vortices and forms elongated structures called side vortices. Above the cylinder roof, a weaker pair of tip vortices occurs but rapidly degrades. This reattachment diminishes the three-dimensionality of the flow, making it more two-dimensional. Accordingly, Rastan et al. (2021) proposed that, in the absence of reattachment (low CR), the near wake displays an arch-shaped coherent structure with staggered legs at the flanks. In this framework, Kumar and Tiwari (2019) conducted a comparative study on the wake structures of three wall-mounted cylinders with different cross sections (circular, triangular, and square) using direct numerical simulations (DNS) at varying Reynolds numbers and as a function of the shear intensity. Despite the fact that AR was the same for all cases, the transition from dipole to quadrupole wake occurred first for the circular cylinder and then for the square and triangular cylinders with changing Reynolds numbers.

To summarize the previous findings, Yauwenas et al. (2019) combined experiments and LES of a wall-mounted square cylinder in a turbulent boundary layer in order to explore the parametric change of the critical AR_c as a function of the AR and the BL thickness. By considering their results with those of other authors such as Wang and Zhou (2009), Bourgeois et al. (2011) and Hosseini et al. (2013), Yauwenas et al. (2019) developed a new diagram of the transition from a dipole to a quadrupole wake as a function of two parameters: the aspect ratio and the boundary-layer thickness. Yauwenas et al. (2019) highlighted the existence of a transition region where both wake configurations

are equally possible, but without providing an analytical expression for critical AR_c.

In conclusion, we provide an accurate analysis of the turbulent flows around finite, wall-mounted square cylinders immersed in a turbulent boundary layer with data support from the TKE budget, the Reynolds stresses and anisotropy-invariant maps (AIM), and using a high-resolution LES simulation at a relatively high Reynolds number. The overall aim is to study the transition from a "dipole" to a "quadrupole" as a function of the aspect ratio (AR), investigated in the past but still an open question when considering the role played at high Reynolds number by the properties of the oncoming turbulent boundary layer. While Yauwenas et al. (2019) focused on the transition from "dipole" to "quadrupole" wake as effect of only the BL thickness and AR, we believe that this classification, based on recent findings, needs to consider additional geometric and turbulent parameters (Vinuesa et al., 2015). Consequently, we propose a brand new conceptual and comprehensive definition of the critical AR_c as a function of Re_θ.

The methodology and numerical setup are extensively discussed and motivated in Section 2. The influence of the aspect ratio (AR) on the wake turbulence is detailed in Section 3, supported by the analysis of anisotropy-invariant maps in Section 3.3, and Reynolds stresses and the turbulent kinetic energy (TKE) budget are discussed in Section 3.4 and Section 3.5, respectively. Conclusions and final considerations are provided in Section 4.

2. Computational setup

A wall-mounted square cylinder immersed in an incompressible turbulent boundary layer is investigated using high-resolution LES. The instantaneous streamwise u, vertical v and spanwise w velocities along the x, y, and z axes, respectively, are Reynolds averaged and decomposed into a mean quantity in time (indicated by $\bar{\cdot}$) $\overline{\mathbf{u}}$ and a turbulent fluctuation $\mathbf{u}'$. The Reynolds stresses are hence denoted by $\overline{u_i' u_j'}$. The coordinate system and the governing equations are dimensionless and scaled by the height of the cylinder h and the free-stream velocity u_∞ of the incoming flow. Thus, the dimensionless time is divided by u_∞/h. Given these definitions, the Reynolds number is $Re_h = u_\infty h/\nu$, where ν is the kinematic viscosity of the flow, and the friction Reynolds number is defined as $Re_\tau = u_\tau \delta_{99}/\nu$, where $u_\tau = \sqrt{\tau_w/\rho}$, τ_w the wall-shear stress and δ_{99} is the boundary-layer thickness. The momentum-thickness-based Reynolds number is $Re_\theta = u_\infty \theta/\nu$, where the momentum thickness is

$$\theta = \int_0^\infty \frac{u}{u_\infty}\left(1 - \frac{u}{u_\infty}\right) \mathrm{d}y. \tag{1}$$

Furthermore, the displacement-thickness-based Reynolds number $Re_{\delta*} = u_\infty \delta^*/\nu$ is expressed as function of

$$\delta^* = \int_0^\infty \left(1 - \frac{u}{u_\infty}\right) \mathrm{d}y. \tag{2}$$

The high-resolution LES are carried out with the open-source code Nek5000, which was developed by Fischer et al. (2008) using the spectral-element method (SEM) as described by Patera (1984). The governing equations are discretized using the $P_n - P_{n-2}$ formulation of the Galerkin projection method, where n represents the maximum polynomial order of the trial function for velocity, while $n-2$ corresponds to the polynomial order for the pressure trial function. The total number of elements is between 210,000 to 240,000 for the cases under studies, with 101 elements in x, 41 elements in y and 24 elements in z, while in proximity of the obstacle the mesh resolution increases. For each element, a 7th-order polynomial following Gauss–Lobatto–Legendre (GLL) quadrature has been considered to properly simulate the multi-scale character of turbulence. The resolution is increased by reducing the size of the elements close to the wall. The mesh follows the criteria proposed by Negi et al. (2018) for the same high-resolution LES implementation. In agreement with the simulations carried out by Atzori et al. (2023), the near-wall resolution follows the guidelines $\Delta x^+ < 18$, $\Delta y^+ < 0.5$, and $\Delta z^+ < 9$. Moving away from the wall, the mesh resolution satisfies the condition $\Delta/\eta < 9$, where $\Delta = (\Delta x \Delta y \Delta z)^{1/3}$, $\eta = (\nu^3/\epsilon)^{1/4}$ is the Kolmogorov scale and ϵ is the local isotropic dissipation. Here, the overall resolution refers to the fine resolution with considering the spectral-element nodes. This makes the present resolution close to the that of a DNS (Negi et al., 2018). For the sake of completeness, the mesh for the case with aspect ratio AR=3 is reported in Fig. 1 (panel a). In the same figure, we also report the ratio Δ/η at $z = 0$. The high-resolution LES is based on the time relaxation described by Negi et al. (2018) for the approximate deconvolution model. The governing equations include a forcing term defined as the following high-passed filtered velocity:

$$\mathcal{H}(\widetilde{u}_i) = \chi \sum_{k=0}^{N} \gamma_k \alpha_k P_k, \tag{3}$$

where $\tilde{u}$ is the filtered velocity, χ is the filter weight, while P_k and α_k denote the base polynomials and the corresponding coefficients, respectively. Hereinafter, the symbol $\tilde{\cdot}$ denotes the filtered quantities. The filter transfer function is:

$$\gamma_k = \begin{cases} 0 & k_s \le k_{s_c}, \\ \left(\dfrac{k_s - k_{s_c}}{N - k_{s_c}}\right)^2 & k_s > k_{s_c}, \end{cases} \tag{4}$$

where k_s is the wave number and k_{s_c} is the cut-off wave number. The governing equations are non-dimensionalized with h and u_∞.The forcing term defined in this way is purely dissipative. The Navier–Stokes equations for the filtered velocity $\widetilde{u}_j$ then become:

$$\frac{\partial \widetilde{u}_i}{\partial t} + \widetilde{u}_j \frac{\partial \widetilde{u}_i}{\partial x_j} = -\frac{\partial \tilde{p}}{\partial x_i} + \frac{1}{Re_h}\frac{\partial^2 \widetilde{u}_i}{\partial x_j \partial x_j} - \mathcal{H}(\widetilde{u}_i), \tag{5}$$

$$\frac{\partial \widetilde{u}_i}{\partial x_i} = 0, \tag{6}$$

Following the resolution criteria reported above, this methodology has been shown to yield excellent agreement for the mean velocity, the Reynolds-stress tensor and the turbulent-kinetic-energy budget. The domain size is $L_{x_1} = 10h, L_{x_2} = 6h, L_y = 3h$ and $L_z = 4h$ in the x, y, z directions, respectively (see sketch in Fig. 2). It is worth noting that, in the present analysis, the domain dimensions are considerably smaller compared to those reported in previous studies (Saeedi et al., 2014; Vinuesa et al., 2015; Zhang et al., 2017; Rastan et al., 2019). This reduction in the domain size can be justified by the outflow boundary conditions imposed in the present analysis (see the following).

At the inlet, an incoming Blasius boundary layer profile with a displacement-thickness-based Reynolds number $Re_{\delta*} = 450$ is imposed. The transition from laminar to turbulent flow is forced by a numerical tripping consisting of a numerical random volume forcing to model the presence of an experimental trip. The tripping forcing is applied along a transversal line at $x = -9$. The position and the parameters of the tripping have been calibrated to enable fully-developed turbulent boundary layer before reaching the obstacle. For more details about the tripping function, see Hosseini et al. (2016). At the top boundary we prescribed a uniform freestream velocity and an outflow, leading to a zero-pressure-gradient (ZPG) boundary layer. In the spanwise direction we impose periodic boundary conditions, and at the outflow we set the stabilized condition by Dong et al. (2014). While the downstream domain size (L_{x_2}) may appear relatively small for the purposes of this study, it has been chosen carefully in the light of the Dong outflow condition, which introduces a novel approach for highly truncated unbounded domains. The dimensions of the domain have been meticulously calibrated in both the streamwise and spanwise directions to strike a balance between computational efficiency and result accuracy. At the upper domain boundary ($y = L_y$) a zero-stress condition in the normal direction is imposed for the streamwise velocity component in order to simulate irrotational flow in the outer boundary layer. Both vertical v and spanwise w velocity components are otherwise set to

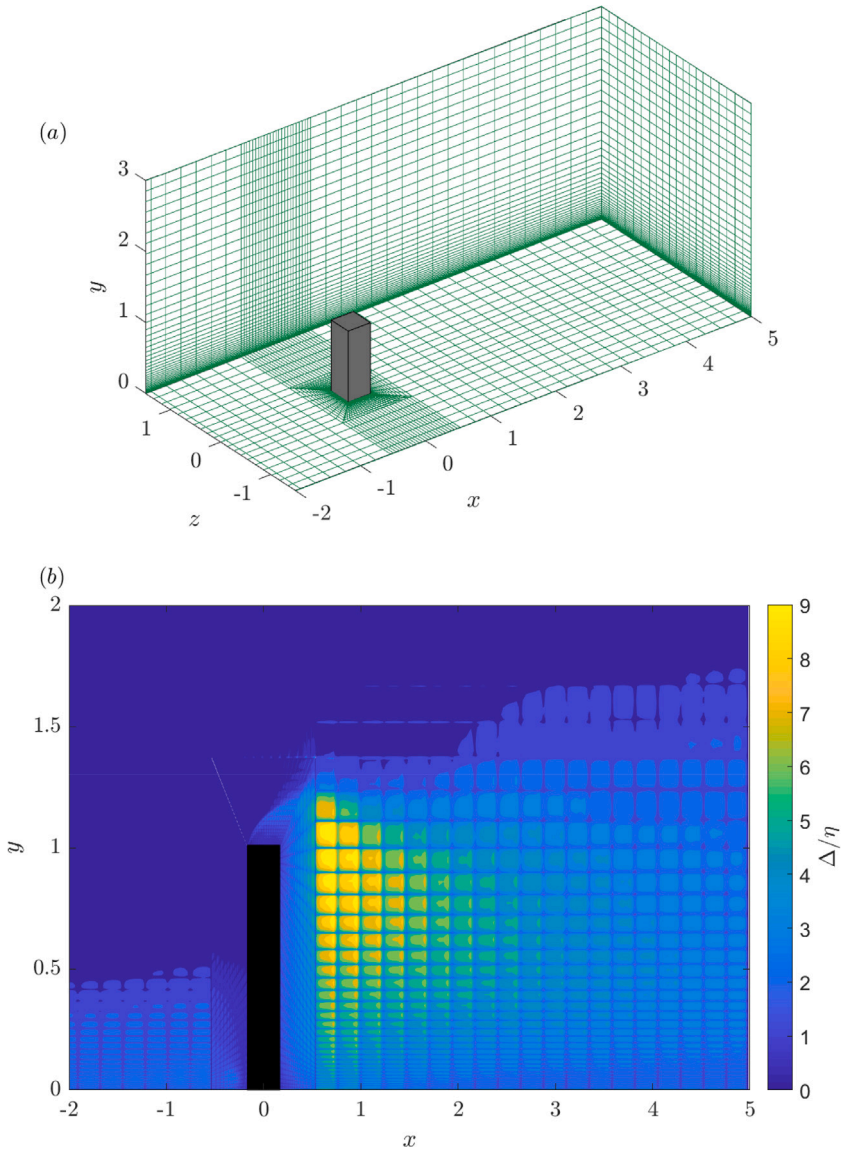

Fig. 1. Three-dimensional view of the mesh at AR=3 (panel a) and Δ/η at $z = 0$ (panel b).

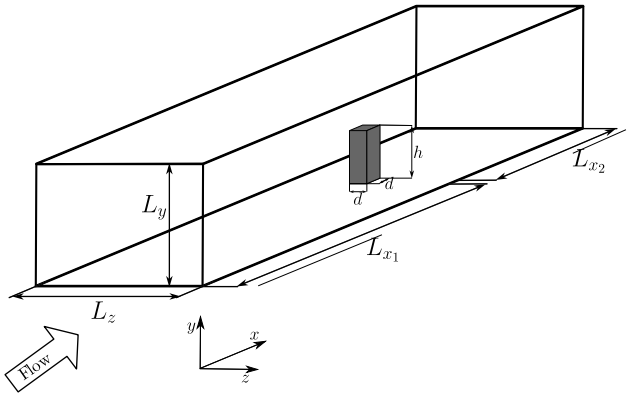

Fig. 2. Sketch of the domain and the obstacle.

zero (Fischer et al., 2008). In the present analysis we report the results for a wall-mounted square cylinder in a turbulent boundary layer with $Re_h = 10{,}000$, corresponding to $Re_\tau \approx 180$ and $Re_\theta \approx 460$ at the location of the obstacle (see Atzori et al. (2023) for additional details). The boundary-layer thickness is computed following the approach proposed by Vinuesa et al. (2016) for APG TBL. In fact, upstream the cylinder, the obstacle generates a small adverse pressure gradient that needs to be considered in the definition of boundary layer thickness. This APG due to the obstacle blockage makes the boundary layer "thick" as δ_{99}/h exceeds the threshold value of 0.3 distinguishing "thin" from "thick" configuration. In this study at the obstacle location, δ_{99}/h and shape factor H are approximately 0.38 and 1.62, respectively, for all cases considered.

In the present paper, four main configurations are studied at different aspect ratios AR = 1, 2, 3, and 4 which are obtained by fixing the height of the cylinders and changing their width. Thus, the incoming turbulent properties are unaltered as well as the boundary-layer thickness with respect to the obstacle height. The cases will be denoted as ARx, where x is the corresponding value of the aspect ratio.

2.1. Oncoming TBL properties

Before focusing on the effect of the aspect ratio on the mean wake configurations, it is pivotal to observe the development of the oncoming

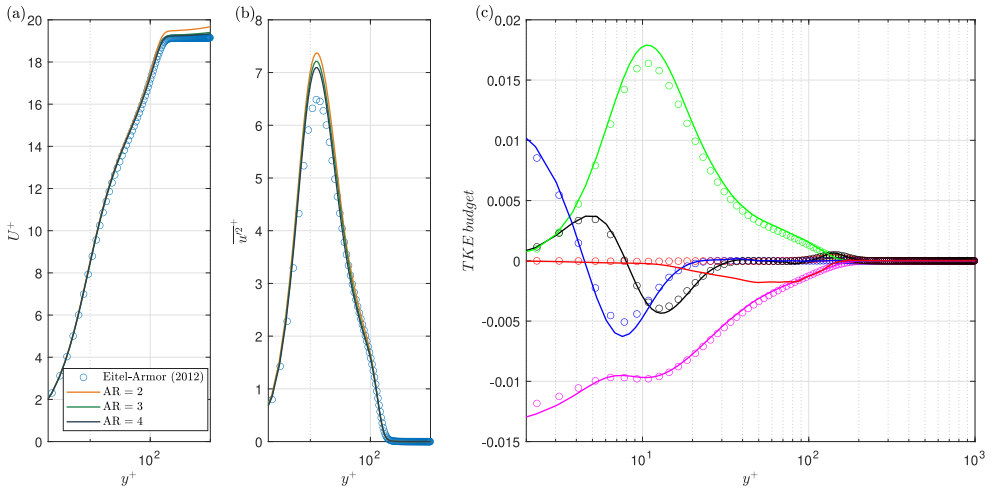

Fig. 3. Inner-scaled mean streamwise velocity U^+ (panel a) and velocity fluctuation $\overline{u'u'}^+$ (panel b) profiles at $x = -4$ and for cases AR2-AR4. The friction Reynolds number considered is $Re_\tau = 168$, corresponding to Re_τ. The production (green), transport (black), viscous diffusion (blue), dissipation (magenta) and pressure correlation (red) terms of the TKE budget are reported in panel (c) only for the case AR2 and compared with the LES from Eitel-Amor et al. (2014) for matching Re_τ. (For interpretation of the references to color in this figure legend, the reader is referred to the web version of this article.)

turbulent boundary layer in front of the obstacle. The mean inner-scaled streamwise velocity U^+ profile at $x = -4$ is reported in panel (a) of Fig. 3 for the cases AR2, AR3 and AR4 and compared with the profile from Eitel-Amor et al. (2014) at matching $Re_\tau = 168$. The present results display a good agreement with the reference velocity profile for all cases considered. It is worth noting that blockage of the obstacle slightly affects the velocity profiles in the outer layer and this explains the differences across the cases AR2-AR4 and with the reference zero-pressure-gradient boundary layer (ZPG BL) (Eitel-Amor et al., 2014). The good agreement with the reference profile not only demonstrates the incoming TBL is properly simulated but also the effectiveness of the numerical tripping formulation by Schlatter and Örlü (2012). The second-order statistics $\overline{u'u'}^+$ are also reported in panel (b) where the present results show higher peaks attributed to the small APG in front of the obstacles. It is interesting to observe that the APG affects the TKE budget (panel c) for the case AR2, in particular for the pressure correlation term that depends on the pressure field (not zero of the APG), but this effect is minor. This confirms that the assumption of ZPG BL upstream the obstacle is reasonable.

3. Effect of AR on the wake structure

Although the effect of AR on the near wake is well-documented in the literature (Sakamoto and Arie, 1983; Wang and Zhou, 2009; Dousset and Pothérat, 2010; Rastan et al., 2017; Zhao et al., 2021), the majority of previous simulations have been conducted at low Reynolds numbers or employed significantly lower resolution at a higher Reynolds number. In the present study, we aim to evaluate the influence of AR on a fully developed turbulent boundary layer without wall modeling. High-resolution LES is employed to better describe the statistical behavior of the wake and to investigate in detail the various terms of the production, transportation, and distribution of turbulence energy throughout the analysis of the TKE budget. It is worth noting that, despite the large amount of experimental and numerical data (Wang and Zhou, 2009; Yauwenas et al., 2019; Zhang et al., 2017), a straightforward comparison is challenging due to the higher Reynolds number of the present study.

3.1. Mean and instantaneous flow field

The mean streamwise and vertical velocity components in the vertical symmetry plane are displayed in Fig. 4. Streamlines are included in the same figure to help the reader with the visualization of the recirculation region behind the obstacle. This figure shows that the more evident effect of AR is on the size of the wake because of the increasing influence of the tip and the base vortices. The occurrence of both tip and base vortices can be outlined by the mean streamwise and vertical velocity components. The tip vortices are associated with a downwash movement in the wake: stronger tip vortices imply a stronger negative vertical velocity, a shorter wake, and hence a higher streamwise velocity. Similarly, the base vortices are associated with an upwash movement, starting from the edge between the obstacle and the bottom surface and extending for a short portion of the wake. For the case AR1, the tip vortices are weak, as evidenced by the fact that the negative velocity in the panel (b) is weaker than the other cases. Additionally, base vortices do not emerge because there is not a positive vertical velocity in the bottom part of the wake. Thus, the wake is stronger and exhibits a single recirculation bubble that occupies the entire wake length until $x = 2$, where the impingement point occurs at the bottom wall. The impingement point, defined by Zhang et al. (2017) as the saddle point where both upwash and downwash coexist, for the case AR1 (panel a) is located at the bottom wall and slightly moves upwards for higher AR. For increasing AR, the wake shrinks in both x and y due to the stronger tip vortices associated with a downwelling motion (see panels f and h). The recirculation bubble is reduced in size, and a second recirculation zone occurs in the lower wake region. The reduction of the wake length can be correlated with the streamwise location of the impingement point from $x = 2$ for AR1 to $x = 1.5$ for AR2 and $x = 1$ for both AR3 and AR4. The change in the wake structure, from a dipole to a quadrupole wake, can also be described by observing how the y coordinate of the impingement point that moves from the wall (panel a) to the center of the wake (panels e and g). As observed by Zhang et al. (2017), the vertical shift of the impingement point is due to the upwash movement produced by the separation of the base vortices from the bottom edge of the cylinder. In this context, a similar behavior in the change of the wake configuration has been observed by Zhao et al. (2021), who carried out a series of simulations of square wall-mounted cylinders in a turbulent boundary layer at increasing Re_h while its AR is fixed to 4. For increasing Reynolds number, the wake of the wall-mounted cylinder changes, and the impingement point moves from the center of the wake (for $Re_h = 100$) to the wall (for $Re_h = 500$). This suggests that both the turbulence characteristics of the incoming flow and the AR are important. For case AR1, the flow detaches at the upper edge and reattaches on the roof, forming a small and weak recirculation region. For AR2–AR4, the flow does not reattach on the roof because of the shorter width of the cylinders. In front of the

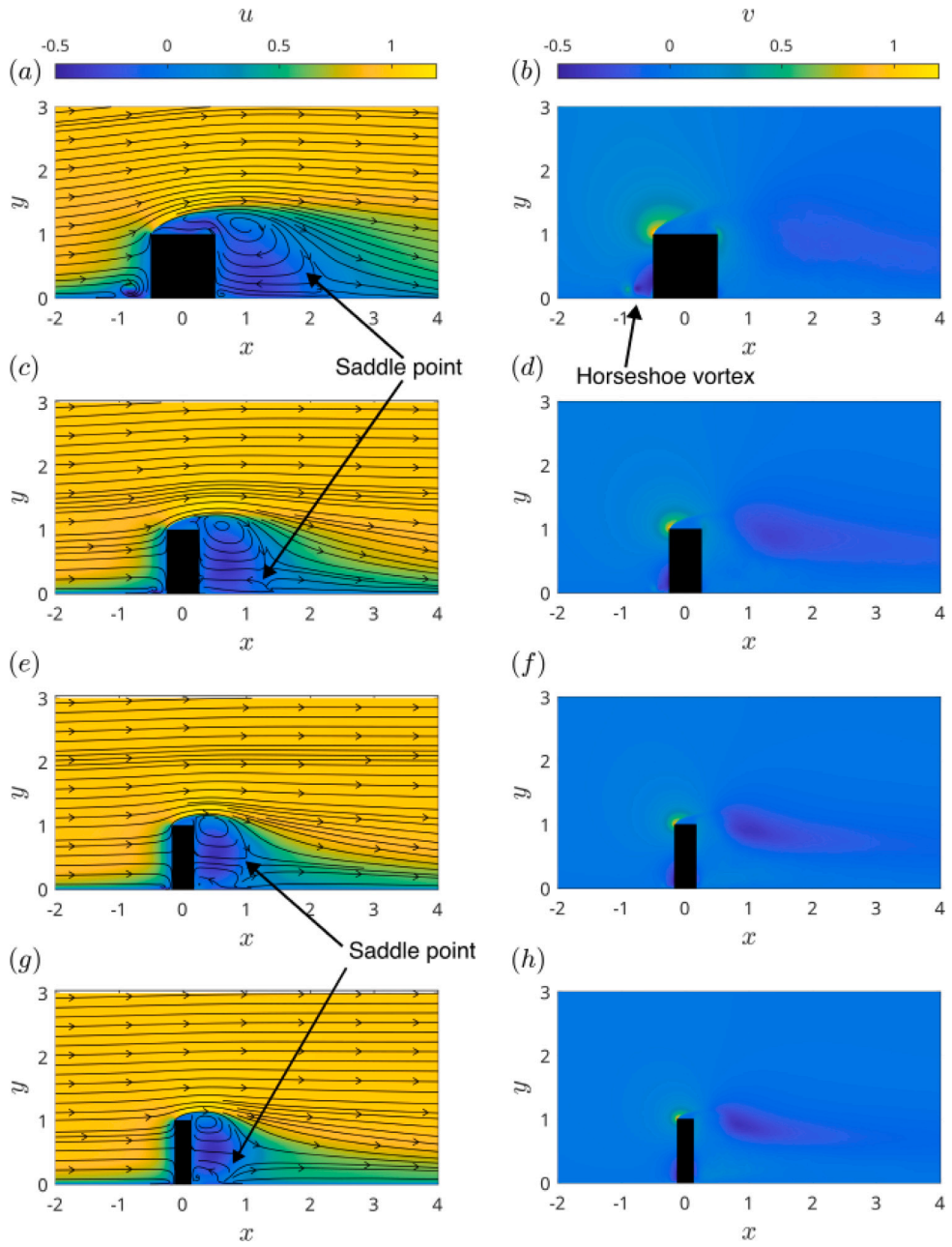

Fig. 4. Mean streamwise (left) and vertical (right) velocity components for the cases AR1 (a, b), AR2 (c, d), AR3 (e, f) and AR4 (g, h). The streamlines in the left panels illustrate the recirculation bubbles inside the wake.

obstacle, a horseshoe vortex emerges. Its size is bigger for AR1 than AR4, where the position of the horseshoe vortex moves downstream until it becomes not discernible from the base vortices. The horseshoe vortex surrounds the sides of the obstacle, causing a downward flow within the vertical tails on either side of the obstacle (Hussein and Martinuzzi, 1996).

In the right panels of Fig. 4, the vertical velocity is broadly similar for all cases studied since the separation region remains constant across all the cases. The maximum positive velocity occurs at the front edge of the roof where the flow detaches, while the outer part of the wake displays a negative v as a result of the tip vortices (see panels f and h). Due to this negative velocity, the wake captures the high-energetic flow at the outer layer and transports it to the core of the wake. The consequences of this mechanism will be clear when analyzing the production term of the TKE budget (see Section 3.5 for more details). The magnitude of the negative vertical velocity is larger for AR1 (panel b), but its intensity is weaker than that of cases AR3 (panel f) and AR4 (panel h). In addition, for the cases AR3 and AR4, in panels (f) and (g) respectively, a positive velocity is barely visible at the bottom part of the wake; note that this is a clear effect of the base vortices.

The time-averaged streamwise vorticity $\Omega_x = \partial w/\partial y - \partial v/\partial z$ at $x = 0$ (left panels) 0.25 (central-left panels) 0.5 (central-right panels) and 0.75 (right panels) is reported in Fig. 5 for the cases AR1 to AR4, arranged from the top to the bottom row. The streamwise vorticity is here utilized to depict the size and the strength of the mean turbulent structures. In particular, the cases AR1 (first row) AR2 (second row) only the tip vortices are observed while at the bottom the footprints of two pairs of horseshoe vortices are discernible in agreement with the conclusion by Zhang et al. (2017). It is worth noting that Zhang et al. (2017) also discerned into two types of tip vortices as primary and secondary vortices produced by the leading and trailing edge, respectively. For increasing AR the horseshoe vortices become progressively

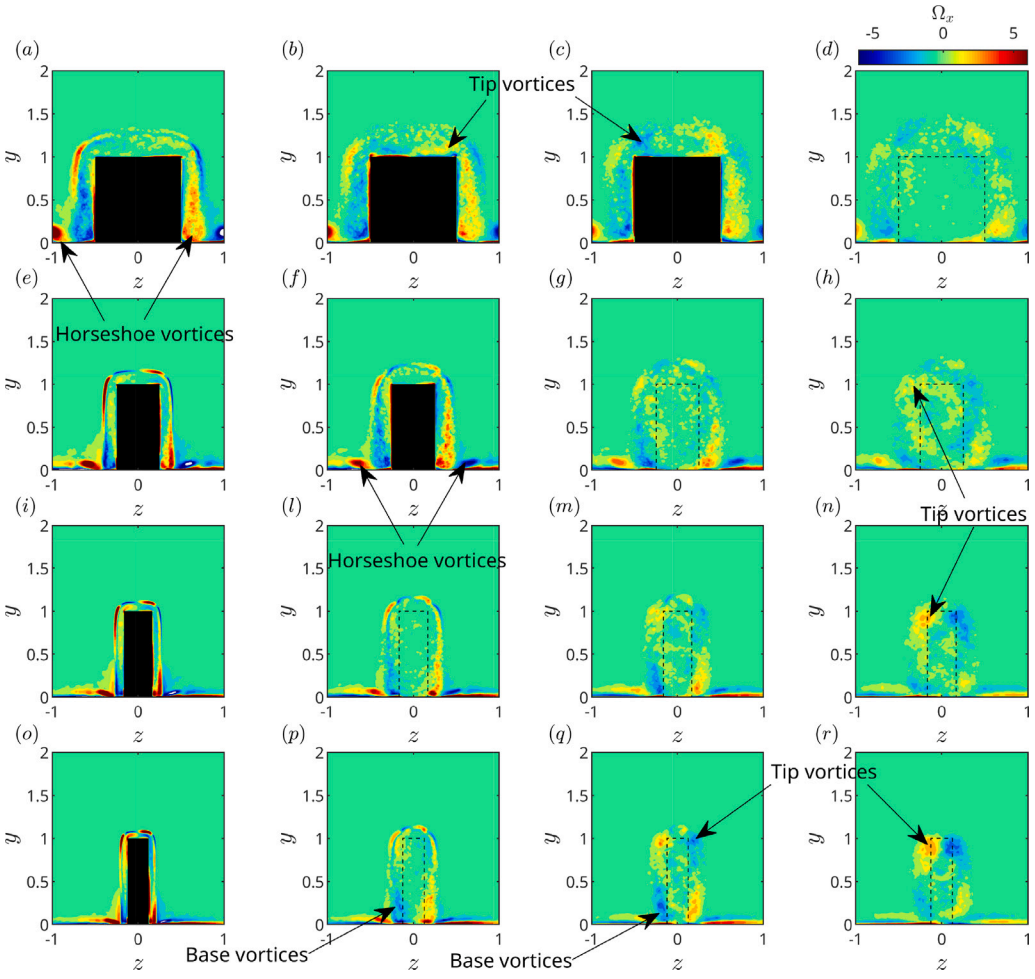

Fig. 5. Contours of the Streamwise vorticity Ω_x at $x = 0$ (left) $x = 0.25$ (center-left) $x = 0.5$ (center-right) and $x = 0.75$ (right) for the cases AR1-AR4 moving from the top to the bottom. Ω_x varies from −6 to 6. Horseshoe, arch, tip and base vortices are properly indicated in the figure.

smaller and move closer to the bottom surface, flattening out. As largely anticipated in the previous section, only the cases AR3 and AR4 display the base vortices, more evident at $x = 0.5$ (panels m and n) and $x = 0.75$ (panels q and r). Although at the first sight the horseshoe and base vortices appear similar and indistinguishable, a more detailed analysis reveals that the base vortices occur away form the bottom surface and at a quarter of the wake height (i.e. panel m and panel q). In addition, the horsewhoe vortices developing in the closest proximity of the obstacles have the same rotational direction as the tip vortices from the same side of the cylinder.

The effect of the downstream distance from the obstacle is also evident. At $x = 0$ (center of the obstacle) the tip vortices are still in development and the flow field surrounds the obstacle forming the well-known arch vortex. Moving downstream (from left to the right columns) the arch-type vortex disrupts, the tip and base vortices emerge more clearly. These changes in the time-averaged structures are also justified by the difference in the instantaneous wake field that changes from a symmetric to an antisymmetric vortex shedding.

The instantaneous vortical motions are identified using the λ_2-criterion (Jeong and Hussain, 1995) in Fig. 6. The wake is symmetric for AR1 (panel a) and AR2 (panel b), when AR $<$ AR$_c$, and the wake is defined as a dipole. For AR3 and AR4, the wake is antisymmetric (Kármán vortex shedding). In panels (c) and (d), the wake is a quadrupole, and the base vortices are discernible. Downstream of the obstacle, these turbulent structures produce structures resembling hairpin vortices (Dousset and Pothérat, 2010; Zhang et al., 2017) (panel c) agglomerated into a complex turbulent structure.

In this context, Dousset and Pothérat (2010) performed direct numerical simulations of a wall-mounted square cylinder, immersed in a turbulent flow delimited by a rectangular duct, to investigate the formation of the hairpin vortex for varying Reynolds numbers. Dousset and Pothérat (2010) distinguished between a symmetric shedding ($Re_d = u_\infty d/\nu = 200$), where a single row of the hairpin vortices is placed in the streamwise direction, and antisymmetric vortex shedding ($Re_d > 250$), where the upwash induced by the base vortices forces the hairpin vortices to aggregate in a complex turbulent structure where their parts are barely discernible. This latter wake theory was expanded by Zhang et al. (2017), who observed that for both the symmetric and antisymmetric configurations, the hairpin vortices are the results of the fragmentation of the Reverse-C spanwise vortices due to the interaction between the downwash, the boundary layer and the shear layer. Although the hairpin vortices have been already described for low Reynolds numbers, the wake structures observed in Fig. 6 for higher Reynolds numbers are not related to any of the aforementioned structures. The wake is more chaotic and the only common pattern is the arch-type vortex separating at the cylinder edges.

Describing the wake complexity is not straightforwards. However, the comparison between the instantaneous field and the averaged quantities can demonstrate that studying the changes in the mean flow field can provide info about the unsteady characteristics of the flow field around the high aspect-ratio buildings.

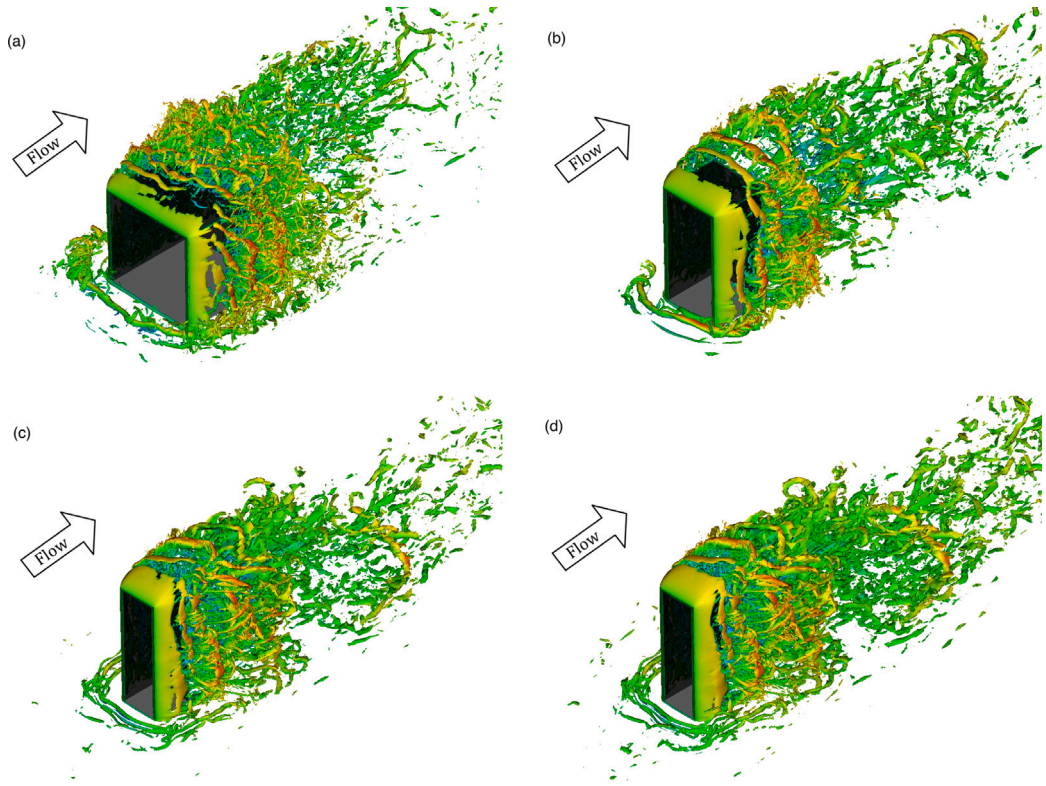

Fig. 6. Instantaneous vortical motions identified by $\lambda_2 = -40$ for the cases AR1 (a), AR2 (b), AR3 (c), AR4 (d). The colormap is the instantaneous streamwise velocity u, ranging from −1.1 (dark blue) to 1.75 (dark red). The arrow indicates the flow direction in each case. (For interpretation of the references to color in this figure legend, the reader is referred to the web version of this article.)

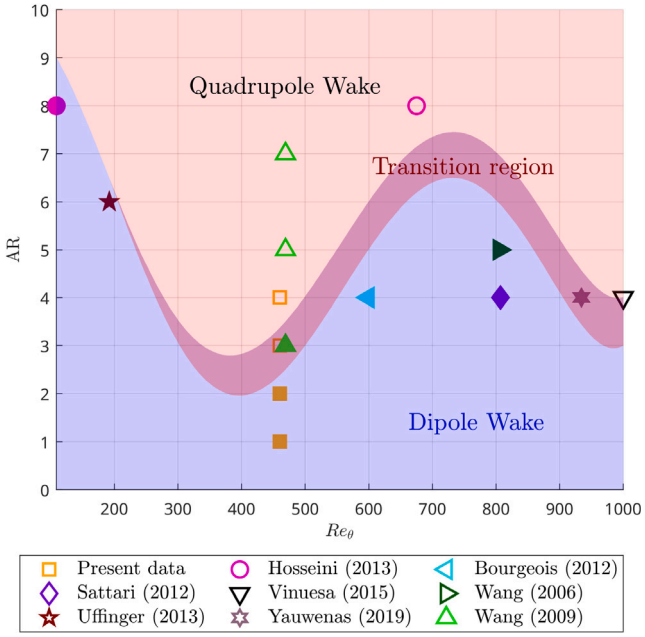

Fig. 7. Comparison of the wake configuration as a function of AR and Re_θ (see figure legend for further details). In the figure, closed symbols denote dipole wakes, while open symbols refer to quadrupole wakes.

3.2. Critical aspect ratio (AR_c)

The present analysis suggests a critical aspect ratio (AR_c) between 2 and 3 where the wake loses its symmetry and Kármán-like vortex shedding is observed. The critical aspect ratio AR_c depends on various flow parameters, such as the momentum thickness, the boundary-layer thickness and the turbulence properties of the incoming boundary layer. The novelty proposed in this study consists of a qualitative description of the transition between dipole and quadrupole wakes, say the AR_c, as a function of $Re_\theta = u_\infty\theta/\nu$, based on the momentum thickness θ. Here, the momentum thickness is preferred because it accounts not only for the boundary-layer thickness, as proposed by many authors in literature (see Yauwenas et al., 2019 and Cao et al., 2022 among others) but also for the turbulent intensity and properties of the incoming boundary layer as reported in the available data in the literature (Hosseini et al., 2013; Bourgeois et al., 2012; Sattari et al., 2012; Vinuesa et al., 2015; Uffinger et al., 2013; Wang et al., 2006). For experiments regarding a turbulent boundary layer developing on a flat plate from Wang et al. (2006), when θ is not available, Re_θ is calculated by considering a naturally developing turbulent boundary layer. The data of wall-mounted square cylinder immersed in a turbulent boundary layer are reported in Fig. 7 where closed symbols denote dipole configurations while open symbols are used for a quadrupole configuration. We distinguish a dipole-wake region (blue area) and a quadrupole-wake region (red area) that overlaps in the transition region (Yauwenas et al., 2019). Yauwenas et al. (2019) observed a transition region where both dipole and quadrupole configurations are possible. Note that Yauwenas et al. (2019) considered only the dependence on the boundary-layer thickness, and not the turbulence properties of the flow. However, it is not enough to characterize the transition between the symmetric and antisymmetric wakes (Yauwenas et al., 2019): as discussed by Vinuesa et al. (2015), the turbulence characteristics of the incoming flow can alter the wake configurations and this discrepancy is sufficient to explain the difference in the wake configuration between the present data and the results produced by Yauwenas et al. (2019). However, the lack of data within the transition region makes it difficult to establish the exact extension of this area. The transition threshold between the dipole and the quadrupole

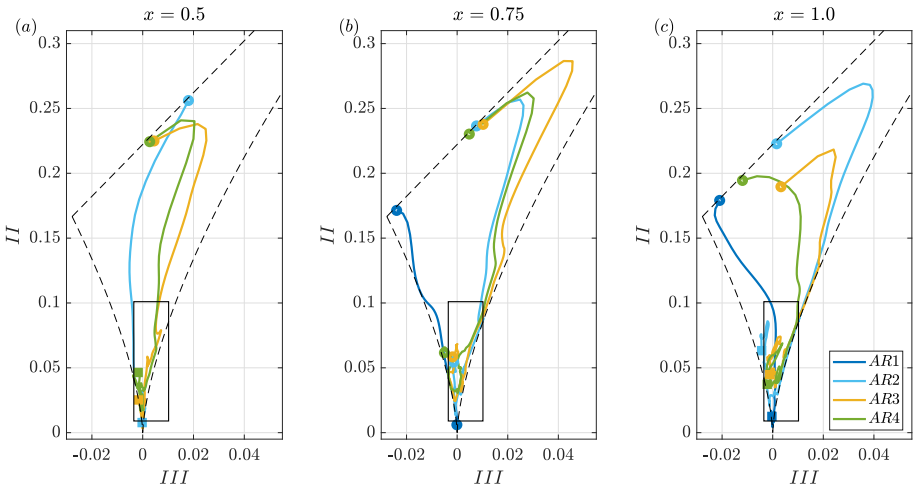

Fig. 8. Anisotropy-invariant maps of cases AR1–AR4 (see legend for further details). The velocity profiles are extracted on the symmetry plane ($z = 0$) and along the vertical direction between $y = 0$ (bottom surface) and $y = 1.0$ (obstacle height) and different locations downstream the cylinder at $x = 0.5$ (panel a), $x = 0.75$ (panel b) and $x = 1.0$ (panel c). The black box delimits the region y in [0, 0.5]. The black dashed lines are the theoretical limits of the II-III which definitions are reported in Eq. (8) (Lumley and Newman, 1977).

wake configuration changes as a function of Re_θ and the AR critical, between $Re_\theta = 460$ and 1000, increases with the Reynolds number. The dependence of the AR_c on the Reynolds number is well known in the literature and largely investigated by other authors, Wang and Zhou (2009), Zhang et al. (2017) among others. The Fig. 7 summarizes this dependence on the Re_θ. Within a moderate range of Re_θ between 480 and 800, the AR_c increases and its value is between 2–6, in agreement with the literature. However, for lower Re_θ between 100 and 400, the critical value rapidly decreases and the dipole wake has been observed experimentally also for very large AR (Uffinger et al., 2013; Hosseini et al., 2013). On the other hand, AR_c peaks at 5.5 for $Re_\theta = 809$ and a further increase of Re_τ produces a reduction of AR_c that needs to be evaluated. Although the literature regarding wall-mounted square cylinders immersed in turbulent boundary layers under different conditions is reasonably rich, many authors did not report the momentum thickness, a fact that makes it difficult to provide a more accurate and general expression for AR_c at the moment based on Fig. 7. Additional data will be needed to accurately depict this transition region. It is worth noting that the present study does not investigate the effect of the cross-sectional ratio because the CR is constant and equal to 1 for all cases considered in order to have a square section. Although many authors (Rastan et al., 2021; Zargar et al., 2022) have suggested that the CR parameter is important for describing the transition from the dipole to the quadrupole wake. Based on the present findings, this transition can be attributed to the change in the δ_{99}/w ratio. Nevertheless, a comprehensive study of the combination effect of both the cylinder height and width changes is still missing in literature. Extending these theoretical considerations while maintaining a general and speculative viewpoint, we can hypothesize that the transition from dipole to quadrupole wake is proportional to the parameter $\delta_{99}h/(bd)$, where b is the cylinder spanwise width. In fact, as observed by previous papers (Wang and Zhou (2009) among others) h and high Reynolds numbers or δ (Wang et al., 2006) promote the emergence of the base vortices while d and b tend to stabilize the dipole wake (Rastan et al., 2021). In conclusion, this study emphasizes the necessity of standardizing the parameters used to describe the effect of turbulence intensity in the oncoming TBL on the transition between the "dipole" and the "quadrupole" wakes. We propose that the Reynolds number based on momentum thickness (Re_θ) and aspect ratio (AR) are sufficient to accurately characterize this transition.

3.3. Anisotropy-invariant maps

The literature widely demonstrated that the wake of a finite wall-mounted cylinder is three dimensional. These characteristics add complexity to the flow field, making it important to quantify the three-dimensionality. Therefore, the anisotropy-invariant maps (AIM) allow us to visualize the changes in the turbulence distribution across the x, y, and z directions. The anisotropy tensor was originally introduced by Lumley and Newman (1977) as:

$$a_{ij} = \frac{\overline{u_i' u_j'}}{2k} - \frac{\delta_{ij}}{3}. \tag{7}$$

Lumley and Newman (1977) identified three invariants, namely:

$$I = a_{ii}, \qquad II = a_{ij}a_{ji}, \qquad III = a_{ij}a_{in}a_{jn}. \tag{8}$$

The anisotropy-invariant map (AIM) graphically displays the development of the dynamics of turbulence in the II-III space (Lumley and Newman, 1977; Banerjee et al., 2007). The space of the possible II-III values is delimited by the two-component limit (II = 2/9 + 2III) that connects the one-component limit (II = 2/3, III = 2/9), where the turbulent energy is distributed along a single direction, and the two-component axisymmetric limit (II = 1/6, III = −1/36), where the turbulence energy is distributed along two directions. The isotropic limit is given by the conditions II = III = 0, which are connected with the 2D-isotropic case by the axisymmetric contraction limit (II = $3/2(4/3|\mathrm{III}|)^{2/3}$) and to the 1D limit by the axisymmetric expansion limit (II = $3/2(4/3|\mathrm{III}|)^{2/3}$). Using the interpretation proposed by Simonsen and Krogstad (2005), the nature of the anisotropy can be represented as an ellipsoid whose radius and axis are proportional to the Reynolds stress tensor and its eigenvalue. In agreement with this interpretation, the 1D turbulence corresponds to a line, the two-component limit is represented as a plane elliptical disk that becomes a circular disk for the 2D axisymmetric limit, while a prolate (or oblate) spheroid represents the axisymmetric contraction (or expansion) limit (Simonsen and Krogstad, 2005). The limits of the II-III space are reported in panel (a) of Fig. 8 for the sake of clarification.

The AIMs for the cases AR1–AR4 at the longitudinal symmetric plane ($z = 0$) and for the velocity profiles at $x = 0.5$ (panel a), 0.75 (panel b), 1 (panel c) are reported in the same figure. The AIMs display the invariants II and III moving from the two-component limits at the base wall (denoted by the circle) to a 3D isotropic limit at the upper region of the wake (denoted by a square marker). This

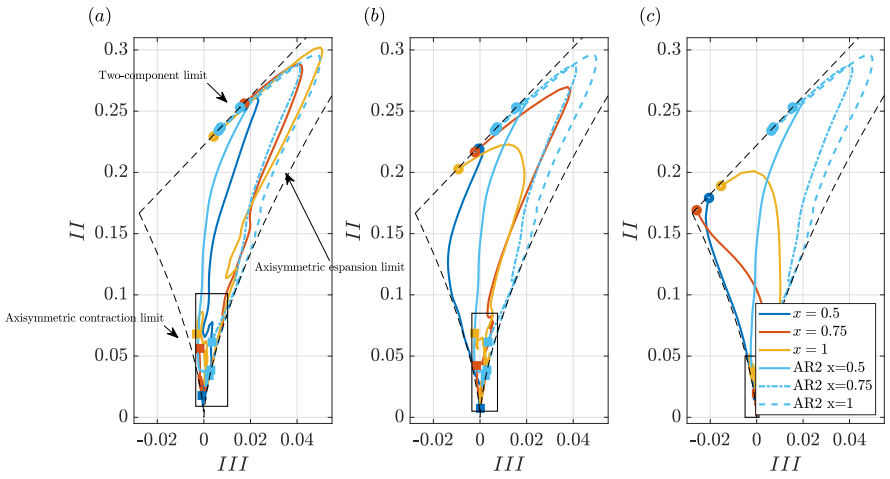

Fig. 9. Comparison between the anisotropy invariant maps for two square cylinders in a row with AR=2 and placed at different gaps indicated as skimming flow (SF) in panel (a), Wake interference (WI) in panel (b) and Isolated Roughness (IR) in panel (c). The curves have been obtained at $x = 0.5$ (blue lines) to $x = 0.75$ (orange lines) and $x = 1$ (yellow lines). The data of AR2 (light blue lines) for $x = 0.5$ (solid) to $x = 0.75$ (dot-dashed) and $x = 1$ (dashed) are superimposed. Data extracted from Atzori et al. (2023). The black dashed lines are the theoretical limits of the II-III (Lumley and Newman, 1977). (For interpretation of the references to color in this figure legend, the reader is referred to the web version of this article.)

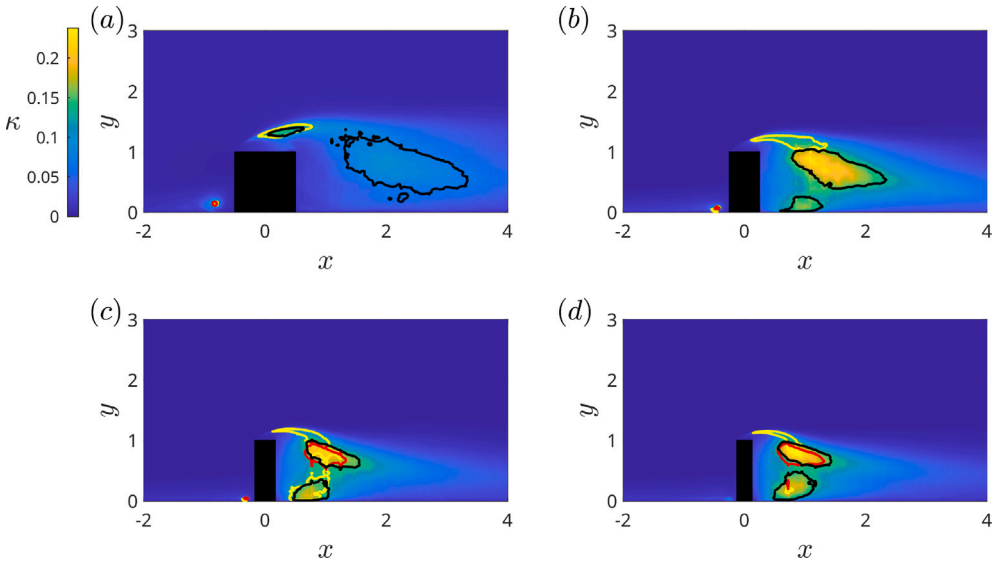

Fig. 10. Turbulent kinetic energy k at the symmetry plane $z = 0$ for the cases AR1 (panel a), AR2 (panel b), AR3 (panel c) and AR4 (panel d). The contour lines delimit the regions of high $\overline{u'u'}$ (yellow) $\overline{v'v'}$ (red) and $\overline{w'w'}$ (black). The lines correspond to a third of the maximum stress. (For interpretation of the references to color in this figure legend, the reader is referred to the web version of this article.)

trend is consistent for all positions considered downstream of the obstacle. Except for the first point at the wall, the wake is highly three-dimensional. However, for the cases AR2–AR4, the turbulence distribution follows the axisymmetric expansion limit. For $x = 0.75$ (panel b), a different trend is observed for the case AR1 where the curve follows the 2D contraction limit. It is worth noting that the case AR2 is the only case displaying an increase in peak magnitude (panels b and d). In the framework of turbulent structures in the urban environment, the effect of the downstream obstacle is more evident when comparing the present analysis with the simulations published by Atzori et al. (2023) for two obstacles in tandem and varying gaps as displayed in Fig. 9. The AIMs from Atzori et al. (2023) for the velocity profiles in the wake of the upfront square cylinder with AR=2 in a two-tandem configuration are included for comparison. Specifically, three configurations have been studied: skimming flow (SF) is shown in panel (a), wake interference (WI) in panel (b), and isolated roughness (IR) in panel (c) at different locations from $x = 0.5$ (blue lines) to $x = 0.75$ (orange lines) and $x = 1$ (yellow lines). These curves are compared with the corresponding maps for an isolated square cylinder (light blue lines). For IR, the AIM closely aligns with the AR2 case at both $x = 0.75$ and $x = 1$, while closer to the obstacle ($x = 0.5$) the two curves differ. The difference between the AIMs increases for WI and SF. In this latter case, the turbulence structures observed between the two cylinders and behind the isolated cylinder are very different. In particular, the AR2 case displays a stronger three-dimensionality. The curve at $x = 0.5$ is interesting because it follows the asymptotic limit and shows a highly two-dimensional energy distribution. Moving downstream, the turbulence becomes three-dimensional, but the peak of the AIM is lower than the AR2 case for all positions considered.

3.4. Reynolds stresses

From the previous analysis, the wake of a wall-mounted square cylinder is three-dimensional and the turbulent energy is not equally distributed across the three reference directions (see Fig. 8). The turbulent kinetic energy $k = 1/2(\overline{u'u'} + \overline{v'v'} + \overline{w'w'})$ in the longitudinal

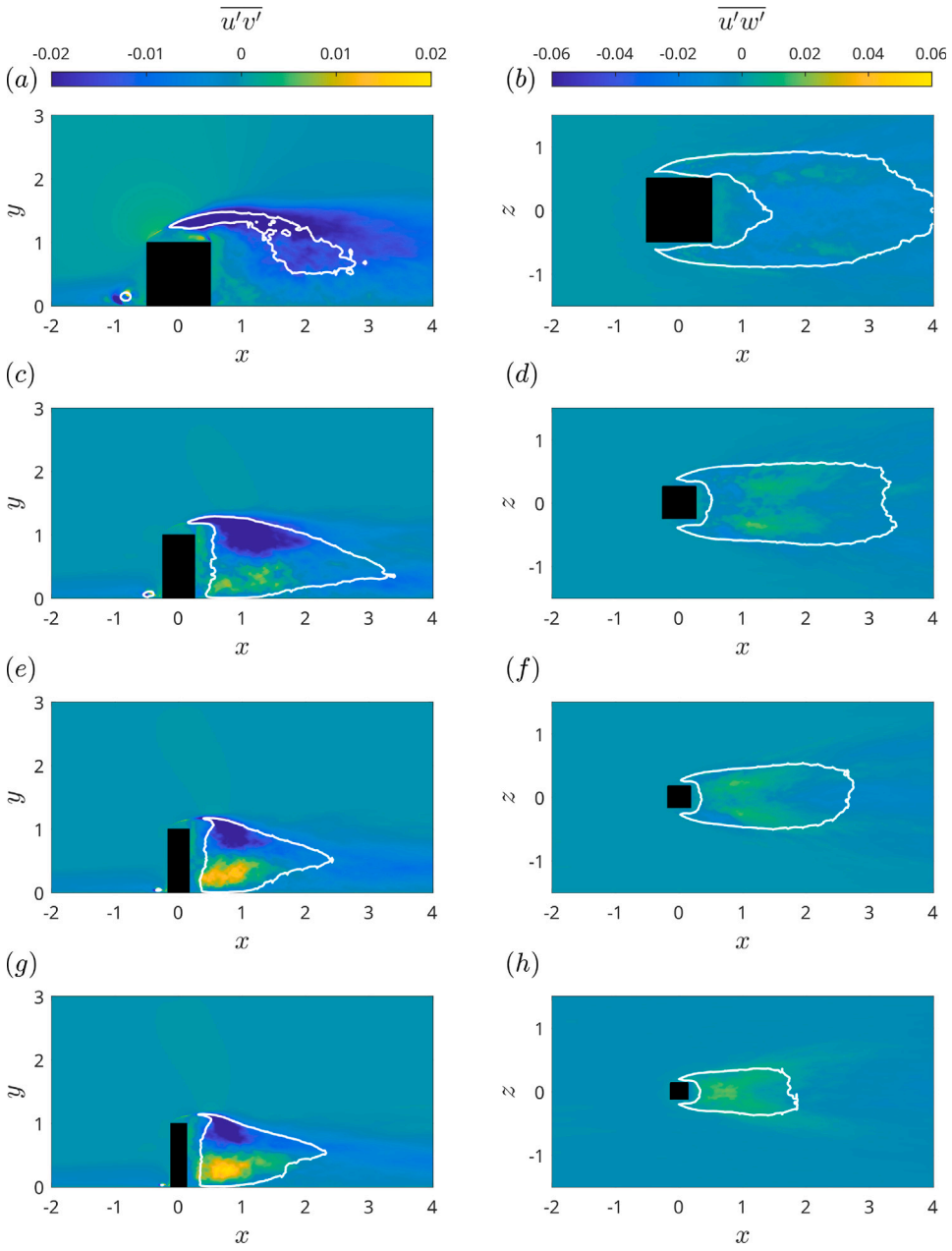

Fig. 11. Contour plots of the shear stresses $\overline{u'v'}$ at $z = 0$ (left column) and $\overline{u'w'}$ at the horizontal plane $y = 0.5$ (right column). The high turbulent kinetic energy k is delimited by the white contour corresponding to 1/3 of the maximum value in the domain for all cases.

symmetric plane ($z = 0$) is first plotted in Fig. 10. The regions of high $\overline{u'u'}$, $\overline{v'v'}$ and $\overline{w'w'}$ are also reported in the same figure in order to highlight the correlations between these quantities and the turbulence peak k. In front of the cylinder, the region of higher turbulent kinetic energy corresponds to the footprint of the horseshoe vortex which size and position depends on the AR. For the cases AR1 (panel a) and AR2 (panel b), the horseshoe vortex is larger because of the stronger adverse pressure region upfront the cylinder induced by the building blockage. For increasing AR (panel c and d), the building blockage decreases, the separation line moves towards the leeward surface of the building and the horseshoe vortex reduces in size. For AR3 (panel c) and AR4 (panel d) the horseshoe vortex is negligible and it does not affect the wake strength.

Apart from the peak of k corresponding to the horseshoe vortex, a second peak emerges above the cylinder roof within the separation region induced by the roof edge. The primary contributor is the streamwise turbulence fluctuation $\overline{u'u'}$ (yellow line), with the other components being negligible or zero. Within the wake, a third, weaker peak is observed in the upper part. This peak aligns with the peak region of $\overline{u'u'}$ (yellow line), $\overline{v'v'}$ (red line), and $\overline{w'w'}$ (black line). For AR3 and AR4, a fourth peak is situated inside the bottom half of the wake, closer to the cylinder base, attributed to the base vortices, with the primary contributors being $\overline{u'u'}$ and $\overline{w'w'}$.

This difference in the turbulence energy can be attributed to the different wake configurations. For AR1 (panel a) and AR2 (panel b) the wake is a dipole, the dominant structure in the wake is the so-called arch-type vortex and the source of the turbulence is located above the cylinder. For the AR3 (panel c) and AR4 (panel d), the peak moves inside the wake region where the most important turbulent structures are the hairpin vortices. The wake shrinks in the spanwise direction, the maximum of k tends to occupy the region behind the obstacle and the maximum contribution is given by $\overline{w'w'}$. The streamwise normal stresses peak above the obstacle for AR1 and AR2 where the flow shows a high-shear region. This is probably due to the interaction

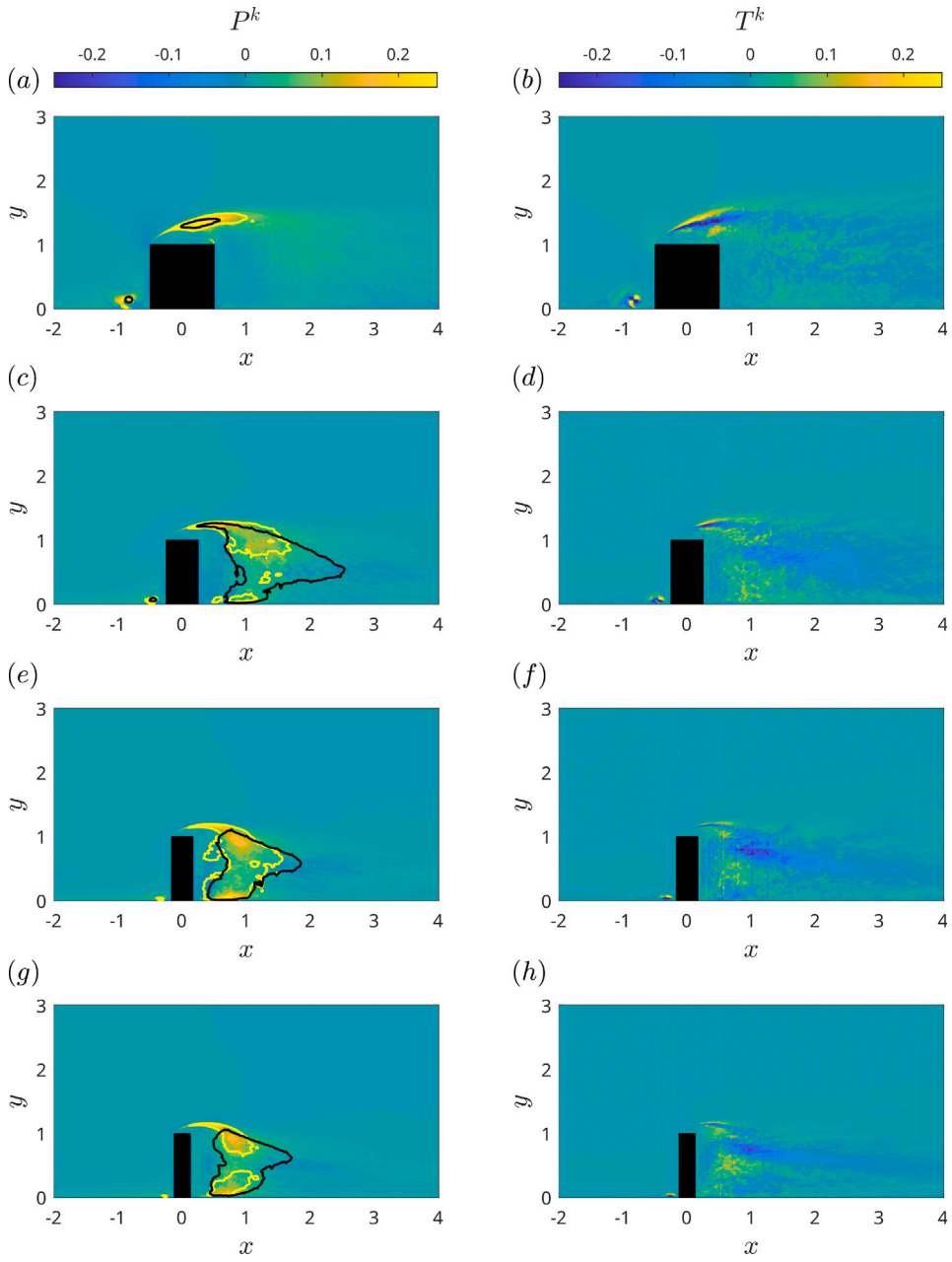

Fig. 12. Production P^k (left column) and transport T^k (right column) terms of the turbulent kinetic energy budget for $z = 0$. The contour lines delimit the peak region of $\overline{u'u'}$ (yellow) and k (black). The cases AR1-AR4 are plotted from the top to the bottom panels. (For interpretation of the references to color in this figure legend, the reader is referred to the web version of this article.)

between the low-momentum flow at the roof of the obstacle and the high-momentum flow in the upper part of the boundary layer. For higher aspect ratios, cases AR3 and AR4, the regions of high $\overline{u'u'}$ above the obstacle are reduced, i.e. the wake is affected by a very strong downwash due to the tip vortices which transports the high-energy flow in the outer part of the boundary layer towards to the low-momentum flow in the wake. This creates a region in the wake where the streamwise momentum $\overline{u'u'}$ is maximum. Inside the wake, $\overline{v'v'}$ is weak and negligible for the case AR1 while it becomes important for higher aspect ratios. The component $\overline{w'w'}$ is equally important inside the wake across all the cases considered in this paper. However, the only difference observed between the cases AR1 (low aspect ratio) and AR4 (high aspect ratio) consists of the extended of the peak region. This region is larger for AR1 because of the wider wake caused by the larger cylinder width, while for AR4 the normal stress $\overline{w'w'}$ displays a secondary peak above the obstacle.

The shear stresses $\overline{u'v'}$ (left column) and $\overline{u'w'}$ (right column) for the cases from AR1 (top panels) to AR4 (bottom panels) are reported in Fig. 11. The white contour delimits the region of high TKE. The shear-stress $\overline{u'v'}$ is very negative in the upper part of the wake. This proves the tendency of the tip vortices to transport downwards the high momentum flow behind the obstacle. The positive $\overline{u'v'}$ is displayed at the base of the cylinder and is less intense than the negative region. Thus, the flow is driven towards the wake center but the intensity is quite weak because of the wall. The positive region is stronger for AR4 than AR1 because of the effect of the base vortices that drive the flow from the base away from the wall. Similarly, the horizontal stress $\overline{u'w'}$ displays one negative (left-hand side of the obstacle) and one positive (right-hand side of the obstacle) region that transport the high-energetic flow towards the wake center. The strongest transport term has been predicted for the case AR4. Although the second-order statistics have been carried out with a sample of at least 150 time units,

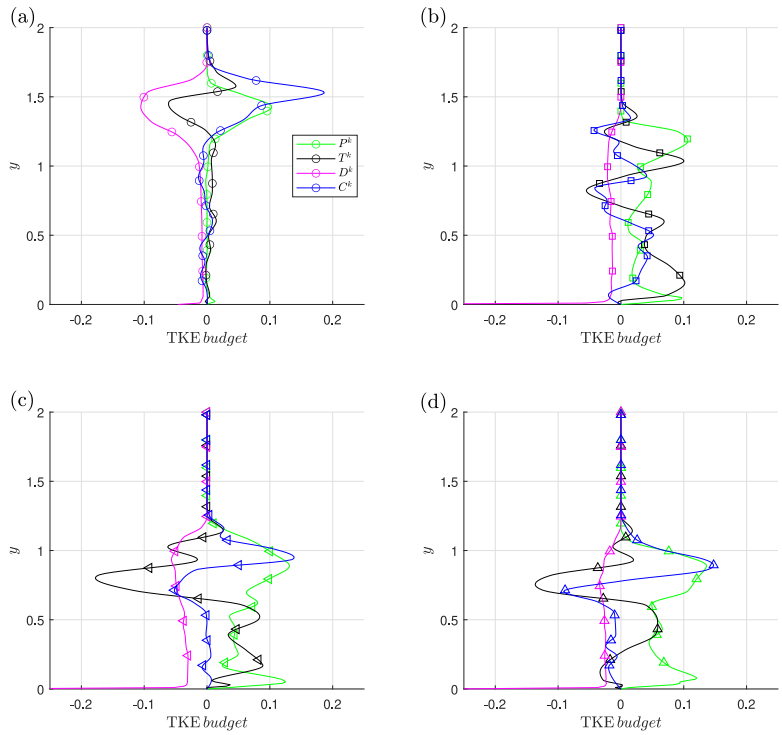

Fig. 13. Profiles of the TKE budget for the cases AR1 (a), AR2 (b), AR3 (c) and AR4 (d) at $x = -1$. In particular, the figure displays the production term P^k (green), transport term T^k (black), viscous diffusion term D^k (magenta) and convective term C^k (blue). (For interpretation of the references to color in this figure legend, the reader is referred to the web version of this article.)

the $\overline{u'w'}$ lacks of symmetry. The time sample is otherwise enough for the statistical convergence of the TKE budget (third-order statistical moments). However, the high computational cost to significantly increase the statistical convergence for all cases is not justified by the purposes of the present paper.

3.5. TKE budget

The turbulent kinetic energy (TKE) budget is reported to display the effect of AR on the regions of high turbulence production, transport and diffusion. Note that the transport equation of the Reynolds-stress tensor is:

$$\frac{\partial}{\partial t}\overline{u_i'u_j'} = \underbrace{-\overline{u_i'u_k'}\frac{\partial u_j}{\partial x_k} - \overline{u_j'u_k'}\frac{\partial u_i}{\partial x_k}}_{P_{ij}} \underbrace{-2\nu\overline{\frac{\partial u_i'}{\partial x_k}\frac{\partial u_j'}{\partial x_k}}}_{\epsilon_{ij}} + \underbrace{\nu\frac{\partial^2}{\partial x_k^2}\overline{u_i'u_j'}}_{D_{ij}} \underbrace{-\frac{\partial}{\partial x_k}\overline{u_i'u_j'u_k'}}_{T_{ij}} + \underbrace{+u_k\frac{\partial}{\partial x_k}\overline{u_i'u_j'}}_{C_{ij}} \underbrace{+-\frac{1}{\rho}\left(\overline{p\frac{\partial u_i'}{\partial x_j}} + \overline{p\frac{\partial u_j'}{\partial x_i}}\right)}_{\Pi^s_{ij}} \underbrace{-\frac{1}{\rho}\left(\frac{\partial}{\partial x_j}\overline{pu_i'} + \frac{\partial}{\partial x_i}\overline{pu_j'}\right)}_{\Pi^t_{ij}}, \quad (9)$$

where P_{ij} is the production term, ϵ_{ij} is the pseudo dissipation term, D_{ij} refers to the viscous diffusion, T_{ij} refers to the turbulent transport while C_{ij} is the convection term. The pressure strain and the pressure transport are denoted b Π^s_{ij} and Π^t_{ij}. Given the definition of the turbulent kinetic energy (TKE) as $k = \frac{1}{2}\left(\overline{u'u'} + \overline{v'v'} + \overline{w'w'}\right)$, the TKE equation becomes:

$$\frac{\partial k}{\partial t} = 0 = P^k + \epsilon^k + D^k + T^k - \Pi^k - C^k, \quad (10)$$

where each term is given by the trace of the corresponding tensor on the right-hand side of Eq. (9). The production P^k and transport T^k terms are shown in Fig. 12 at the vertical symmetry plane for AR value from 1 (top panels) to 4 (bottom panels). The remaining terms of the TKE budget are not reported for brevity of discussion. The contour lines of the $\overline{u'u'}$ (yellow line) and k (black line) peak regions are also shown. From the figure, both P^k and T^k are negligible in the free stream and assume a nonzero value in proximity to the obstacle and in its wake. In particular, the production term exhibits four strong regions, their size and intensity depend on the aspect ratio (AR): (i) at the roof of the cylinder in the flow separation region, (ii) at the upstream edge of the roof, (iii) upstream of the obstacle in correspondence with the horseshoe vortex, and (iv) at the flank of the cylinders (see Fig. 14). For the case AR1 (panel a), the peak region of P^k extends to the roof of the cylinder but rapidly degrades in the wake, where it assumes a low positive value. For increasing aspect ratio (left column), the positive production term is distorted, and it is deflected downwards in the wake as a side effect of the tip vortices. Meanwhile, the horseshoe moves towards the upfront face of the cylinder, and its contribution to P^k is confined to a very small region at the wall. For the cases AR3 (panel e) and AR4 (panel g), a weak positive region occurs at the bottom wall due to the base vortices. As observed in Fig. 4, the upper portion of the wake captures the high-energetic flow of the outer boundary layer that is transported to the center of the wake. Similarly, at the bottom surface, due to the occurrence of the base vortices for the cases AR3 and AR4, the flow is pushed upward towards the wake core. As a consequence, the wake becomes the major region of turbulence production. Note that P^k is slightly altered and is negative in front of the cylinder and above the roof of the obstacles. It is worth noting that the maximum of P^k broadly coincides with the peak region of $\overline{u'u'}$ (yellow line). The transport term T^k is also shown in Fig. 12, and it exhibits a negative–positive pattern above the obstacles while it is negligible in the wake. Comparing the left panels, the increasing aspect ratio (AR) produces a deformation of the region of negative T^k that extends into the wake behind the obstacle. The horseshoe vortex is barely visible only for the case AR1, while the transport of turbulence induced by the horseshoe vortex in front of the obstacle is negligible for the remaining cases. For a deeper understanding of the AR effect we report the profiles of the TKE budget at $x = -1$ in Fig. 13 for all the cases. At this downstream location, the peaks of the production P^k and the convective C^k terms

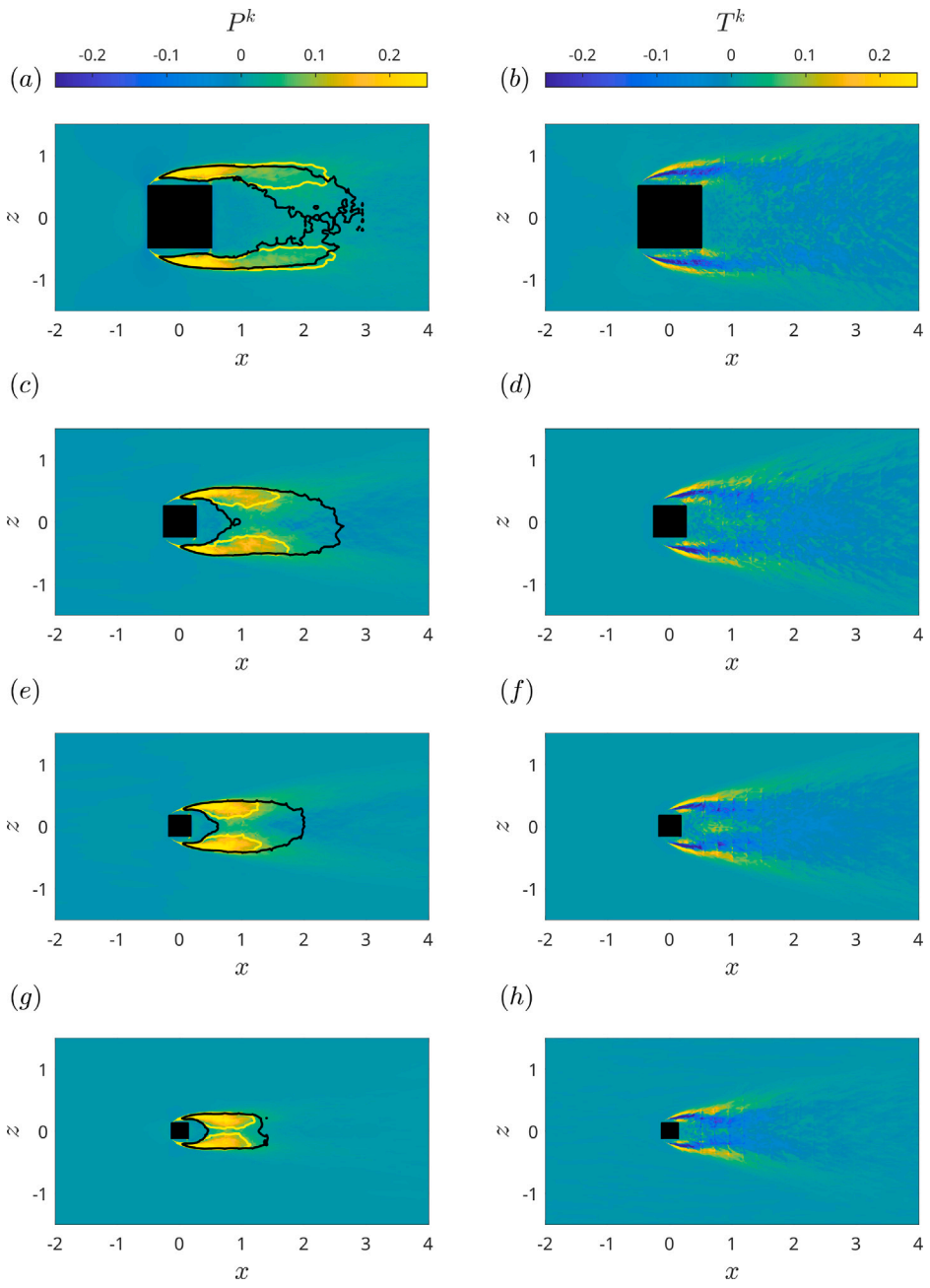

Fig. 14. Production P^k (left column) and transport T^k (right column) terms of the turbulent kinetic energy budget for $y = 0.5$. The contour lines delimit the peak region of $\overline{u'u'}$ (yellow) and k (black). The cases AR1-AR4 are plotted from the upper to the bottom panels. (For interpretation of the references to color in this figure legend, the reader is referred to the web version of this article.)

for the case AR1 (panel a) are situated slightly above the obstacle. However, for increasing AR, the peak of the turbulence production moves downwards and it becomes slightly stronger. A secondary peak occurs for the cases AR3 (panel c) and AR4 (panel d), balanced by the transport term T^k. This quantitatively proves the importance of the turbulence production within the wake for larger AR. It is also worth noting that, for the case AR1 (panel a) the viscous diffusion D^k is slightly negative all along y direction. For the remaining cases, D^k is constant and negative, that is more prominent and playing a more significant role than the convective phenomenon.

The P^k and T^k in the horizontal plane at $z = 0.5$ are finally reported in Fig. 14. The figure displays a region of high turbulence production at the flank of the obstacles. The turbulence produced within this region is then transported inside the wake by the transport term that shows a positive/negative pattern. For the cases AR2 (panel c) to AR4 (panel g), the positive regions of P^k are deflected from the flank towards the wake center. Similarly, the term T^k has two peak regions at the flank of the obstacles, while for increasing aspect ratio, the wake displays a negative transport term. The present findings indicate that the turbulence production is associated with the streamwise shear stress regardless the aspect ratio, suggesting that, from the trajectory optimization perspective, it is convenient to avoid these regions. The case AR1 is the only one that does not display positive production in the wake because it is the only case where the flow reattaches at the roof, the tip vortices are less intense, and their influence on the wake is weak. On the contrary, for the cases AR3 and AR4, the tip and base vortices are stronger and they mainly impact on the turbulence generation in the wake. From a physical standpoint, the examination of the TKE budget corroborates the idea that the turbulence is initially generated in the flow-separation region and is subsequently transported

into the wake. Here, both the tip and base vortices are strongly related to the production of turbulence.

4. Conclusions

The present study investigates the influence of aspect ratio (AR) on the wake structure of a wall-mounted square cylinder immersed in a turbulent boundary layer with Re_h = 10,000, employing high-resolution LES simulations with the open-source software Nek5000. Four configurations are studied at different AR values (1, 2, 3, and 4) to gain insights into the turbulence wake behavior. The change in AR has been achieved by altering the width of the square cylinder to maintain the ratio of the incoming boundary-layer thickness and the obstacle height constant. This approach differs from Yauwenas et al. (2019), in which the change in the AR is achieved by changing the cylinder height. However, the change in the cylinder height causes a different degree of interaction between the incoming BL and the obstacle, and consequently, at similar AR values, the time-averaged turbulent structures can be significantly different. This effect is not investigated in the present paper.

Our findings align with the empirical interpretation by Wang and Zhou (2009) regarding the roles of tip, base, and spanwise vortices in the wake. A key contribution of this work is the identification of a critical aspect ratio AR_c between 2 and 3, where the wake regime changes from a dipole to a quadrupole configuration.

In this study, we introduce a novel framework to describe the dipole-to-quadrupole transition in terms of Re_θ and AR_c, which incorporates the effects of both boundary-layer thickness and turbulence intensity, which has not been formally described in prior research. This framework combines the present results with data from the literature and delineates the regions corresponding to dipole, quadrupole, and transitional wake configurations as a function of Re_θ, addressing a gap in previous research that focused mainly on the boundary-layer thickness alone. While this study does not investigate the effect of the cross-sectional ratio (CR), it highlights the importance of cylinder dimensions in modulating the wake configuration. We thus suggest that the transition could be related to the $\delta_{99}h/(bd)$ ratio, despite further data collection is still necessary. This theoretical dissertation opens up new directions for future research into the combined effects of cylinder height and width on the wake dynamics.

Additionally, we offer new insights into turbulence anisotropy and energy dynamics within the wake. The Reynolds stresses reveal the anisotropic nature of turbulence, particularly near the wake edges, where strong three-dimensionality is observed. This is confirmed by anisotropy-invariant maps (AIM), which indicate that the outer wake region consistently exhibits high turbulence intensity and isotropic characteristics. Analysis of the TKE budget further demonstrates that turbulence production and transport are especially pronounced near the roof and wake regions for AR3 and AR4 configurations, emphasizing the contributions of tip and base vortices to turbulence generation. These findings underscore the role of AR in modulating TKE distribution, notably in enhancing turbulence production and transport in the wake.

Extending the simulations to higher Reynolds numbers, closer to realistic urban conditions, could yield a more comprehensive characterization of urban-flow turbulence but would demand significant computational resources and make it unfeasible to maintain the same accuracy level. Thus, the high-resolution LES setup becomes impractical. Unanswered questions, involving the exploration of additional geometrical parameters such as cross-section aspect ratio (CR) or the boundary-layer thickness, and the correlation between the TKE budget and the trajectory optimization of drones will be addressed in future works.

CRediT authorship contribution statement

Gerardo Zampino: Writing – original draft, Resources, Methodology, Investigation, Data curation. **Marco Atzori:** Formal analysis, Data curation, Conceptualization. **Elias Zea:** Writing – review & editing, Supervision. **Evelyn Otero:** Writing – review & editing, Visualization. **Ricardo Vinuesa:** Supervision, Project administration, Investigation, Funding acquisition, Conceptualization.

Declaration of competing interest

The authors declare the following financial interests/personal relationships which may be considered as potential competing interests: Gerardo Zampino reports financial support was provided by KTH Royal Institute of Technology. If there are other authors, they declare that they have no known competing financial interests or personal relationships that could have appeared to influence the work reported in this paper.

Acknowledgments

This Project has received funding from the European Union's HORIZON Research and Innovation Programme, project REFMAP, under Grant Agreement number 101096698. The computations were carried out at the supercomputer Dardel at PDC, KTH, and the computer time was provided by the National Academic Infrastructure for Supercomputing in Sweden (NAISS).

Data availability

All the data will be available in the following open-access repository after the article is published:
https://www.vinuesalab.com/databases/.

References

Atzori, M., Torres, P., Vidal, A., Le Clainche, S., Hoyas, S., Vinuesa, R., 2023. High-resolution simulations of a turbulent boundary layer impacting two obstacles in tandem. Phys. Rev. Fluids 8, 063801.

Banerjee, S., Krahl, R., F., D., Zenger, C., 2007. Presentation of anisotropy properties of turbulence, invariants versus eigenvalue approaches. J. Turb. 8, N32.

Bourgeois, J.A., Sattari, P., Martinuzzi, R.J., 2011. Alternating half-loop shedding in the turbulent wake of a finite surface-mounted square cylinder with a thin boundary layer. Phys. Fluids 23, 095101.

Bourgeois, J.A., Sattari, P., Martinuzzi, R.J., 2012. Coherent vortical and straining structures in the finite wall-mounted square cylinder wake. Int. J. Heat Fluid Flow 35, 130–140.

Cao, Y., Tamura, T., Zhou, D., Bao, Y., Han, Z., 2022. Topological description of near-wall flows around a surface-mounted square cylinder at high Reynolds numbers. J. Fluid Mech. 933, A39.

Chen, G., Li, X.-B., Sun, B., Liang, X.-F., 2022. Effect of incoming boundary layer thickness on the flow dynamics of a square finite wall-mounted cylinder. Phys. Fluids 34, 015105.

Dong, S., Karniadakis, G., Chryssostomidis, C., 2014. A robust and accurate outflow boundary condition for incompressible flow simulations on severely-truncated unbounded domains. J. Comput. Phys. 261, 83–105.

Dousset, V., Pothérat, A., 2010. Formation mechanism of hairpin vortices in the wake of a truncated square cylinder in a duct. J. Fluid Mech. 653, 519–536.

Eitel-Amor, G., Örlü, R., Schlatter, P., 2014. Simulation and validation of a spatially evolving turbulent boundary layer up to Reθ=8300. Int. J. Heat Fluid Flow 47, 57–69.

El Hassan, M., Bourgeois, J., Martinuzzi, R., 2015. Boundary layer effect on the vortex shedding of wall-mounted rectangular cylinder. Exp. Fluids 56, 33.

Fischer, P., Lottes, J., Kerkemeier, S., 2008. NEK5000: Open source spectral element CFD solver. https://nek5000.mcs.anl.gov/.

Goswami, S., Hemmati, A., 2022. Mechanisms of wake asymmetry and secondary structures behind low aspect-ratio wall-mounted prisms. J. Fluid Mech. 950, A31.

Hosseini, Z., Bourgeois, J.A., Martinuzzi, R.J., 2013. Large-scale structures in dipole and quadrupole wakes of a wall-mounted finite rectangular cylinder. Exp. Fluids 54, 1595.

Hosseini, S., Vinuesa, R., Schlatter, P., Hanifi, A., Henningson, D., 2016. Direct numerical simulation of the flow around a wing section at moderate Reynolds number. Int. J. Heat Fluid Flow 61, 117–128.

Hussein, H.J., Martinuzzi, R.J., 1996. Energy balance for turbulent flow around a surface mounted cube placed in a channel. Phys. Fluids 8, 764–780.

Jeong, J., Hussain, F., 1995. On the identification of a vortex. J. Fluid Mech. 285, 69–94.

Kawamura, T., Hiwada, M., Hibino, T., Mabuchi, I., Kumada, M., 1984. Flow around a finite circular cylinder on a flat plate : Cylinder height greater than turbulent boundary layer thickness. Bull. JSME 27 (232), 2142–2151.

Kumar, P., Tiwari, S., 2019. Effect of incoming shear on unsteady wake in flow past surface mounted polygonal prism. Phys. Fluids 31, 113607.

Lumley, J.L., Newman, G., 1977. The return to isotropy of homogeneous turbulence. J. Fluid Mech. 82, 161.

Negi, P., Vinuesa, R., Hanifi, A., Schlatter, P., Henningson, D., 2018. Unsteady aerodynamic effects in small-amplitude pitch oscillations of an airfoil. Int. J. Heat Fluid Flow 71, 378–391.

Patera, A.T., 1984. A spectral element method for fluid dynamics: Laminar flow in a channel expansion. J. Comput. Phys. 54, 468.

Porteous, R., Moreau, D.J., Doolan, C.J., 2014. A review of flow-induced noise from finite wall-mounted cylinders. J. Fluids Struct. 51, 240–254.

Rastan, M., Shahbazi, H., Sohankar, A., Md., M.A., Zhou, Y., 2021. The wake of a wall-mounted rectangular cylinder: Cross-sectional aspect ratio effect. J. Wind. Eng. Ind. Aerodyn. 213, 104615.

Rastan, M.R., Sohankar, A., Alam, M.M., 2017. Low-Reynolds-number flow around a wall-mounted square cylinder: Flow structures and onset of vortex shedding. Phys. Fluids 29, 103601.

Rastan, M.R., Sohankar, A., Doolan, C., Moreau, D., Shirani, E., Alam, M.M., 2019. Controlled flow over a finite square cylinder using suction and blowing. Int. J. Mech. Sci. 156, 410–434.

Saeedi, M., LePoudre, P.P., Wang, B.C., 2014. Direct numerical simulation of turbulent wake behind a surface-mounted square cylinder. J. Fluids Struct. 51, 20–39.

Sakamoto, H., Arie, M., 1983. Vortex shedding from a rectangular prism and a circular cylinder placed vertically in a turbulent boundary layer. J. Fluid Mech. 126, 147–165.

Sattari, P., Bourgeois, J.A., Martinuzzi, R.J., 2012. On the vortex dynamics in the wake of a finite surface-mounted square cylinder. Exp. Fluids 52 (5), 1149–1167.

Schlatter, P., Örlü, R., 2012. Turbulent boundary layers at moderate Reynolds numbers: inflow length and tripping effects. J. Fluid Mech. 710, 5–34.

Simonsen, A.J., Krogstad, P., 2005. Turbulent stress invariant analysis : Clarification of existing terminology. Phys. Fluids 17, 088103.

Sumner, D., Heseltine, J., Dansereau, O., 2004. Wake structure of a finite circular cylinder of small aspect ratio. Exp. Fluids 37, 720–730.

Uffinger, T., Ali, I., Becker, S., 2013. Experimental and numerical investigation of the flow around three different wall-mounted cylinder geometries of finite length. J. Wind. Eng. Ind. Aerodyn. 119, 13–17.

Vinuesa, R., Bobke, A., Örlü, R., Schlatter, P., 2016. On determining characteristic length scales in pressure-gradient turbulent boundary layers. Phys. Fluids 28 (5), 055101.

Vinuesa, R., Schlatter, P., Malm, J., Mavriplis, C., Henningson, D.S., 2015. Direct numerical simulation of the flow around a wall-mounted square cylinder under various inflow conditions. J. Turb. 16, 555–587.

Wang, H.F., Zhou, Y., 2009. The finite-length square cylinder near wake. J. Fluid Mech. 638, 453–490.

Wang, H.F., Zhou, Y., Chan, C.K., Lam, K.S., 2006. Effect of initial conditions on interaction between a boundary layer and a wall-mounted finite-length-cylinder wake. Phys. Fluids 18, 065106.

Yauwenas, Y., Porteous, R., Moreau, D.J., Doolan, C.J., 2019. The effect of aspect ratio on the wake structure of finite wall-mounted square cylinders. J. Fluid Mech. 875, 929–960.

Zargar, A., Tarokh, A., Hemmati, A., 2022. The unsteady wake transition behind a wall-mounted large-depth-ratio prism. J. Fluid Mech. 952, A12.

Zhang, D., Cheng, L., An, H., Zhao, M., 2017. Direct numerical simulation of flow around a surface-mounted finite square cylinder at low Reynolds numbers. Phys. Fluids 29 (4), 045101.

Zhao, M., Mamoon, A., Wu, H., 2021. Numerical study of the flow past two wall-mounted finite-length square cylinders in tandem arrangement. Phys. Fluids 33 (9), 093603.